Black Sea Journal of Engineering and Science
doi: 10.34248/bsengineering.1951543

Open Access Journal
e-ISSN: 2619 – 8991

Research Article
Volume 9 - Issue 4: 1884-1894 / July 2026

THE EFFECT OF ELECTRODE DIAMETER ON SINGLE-TRACK MORPHOLOGY AND PROCESS WINDOW IN POWDER-BED ARC ADDITIVE MANUFACTURING

Arif BALCI[1], Fatih ALIBEYOGLU[1*]

[1]*Kafkas University, Faculty of Engineering and Architecture, Department of Mechanical Engineering, 36100 Kars, Türkiye*

Abstract: Powder-bed arc additive manufacturing (PBAAM) is a low-cost alternative powder bed fusion process that uses a TIG arc as heat source. This study systematically investigates the effect of electrode diameter (φ = 0.6, 0.8 and 1.0 mm) on single-track morphology and process window in inclined-bed PBAAM of 316L stainless steel powder. Twenty-seven full-factorial combinations of three current levels (I = 20, 25, 30 A) and three travel speeds (v = 2, 3, 4 mm/s) were evaluated using an image analysis framework based on Otsu thresholding with expert manual correction. Maximum gap length (L_{gap}) and width coefficient of variation ($CV = \sigma_w/\bar{w}$) metrics were compared across six threshold scenarios (S1–S6); S5 (L_{gap}) = 0.50 mm, CV = 0.15) was identified as the most appropriate combination based on physical justification and literature consistency. Process map analysis revealed travel speed v as the most critical parameter governing the process window: at v = 2 mm/s, 9/9 combinations (100%) produced continuous tracks; at v = 4 mm/s, only 5/9 (56%) were continuous. Multiple linear regression models achieved R^2 = 0.626 for mean track width w̄ and R^2 = 0.562 for CV. Electrode diameter φ significantly affects track width (β_φ = 0.762, p = 0.019) but has no significant linear effect on width uniformity CV (p = 0.955); CV is primarily governed by I and v. The φ = 0.8 mm electrode confined all Fragmented/Balling combinations to v = 4 mm/s only and produced approximately 35% lower mean CV (0.184) than the other two electrode diameters for continuous tracks.

Keywords: Electrode diameter, Single-track morphology, Process window, Image analysis, Regression model, 316L stainless steel

***Corresponding author:** Kafkas University, Faculty of Engineering and Architecture, Department of Mechanical Engineering, 36100 Kars, Türkiye
E mail: falibeyoglu@kafkas.edu.tr (F. ALIBEYOGLU)
Arif BALCI https://orcid.org/0000-0002-4932-9654
Fatih ALIBEYOGLU https://orcid.org/0000-0002-0323-3630

Received: May 15, 2026
Accepted: July 02, 2026
Published: July 15, 2026

Cite as: Balcı, A., & Alibeyoğlu, F. (2026). The effect of electrode diameter on single-track morphology and process window in powder-bed arc additive manufacturing. *Black Sea Journal of Engineering and Science*, 9(4), 1884-1894.

1. Introduction

Metal additive manufacturing technologies have gained widespread adoption across high-value sectors including aerospace, biomedical, energy and tooling due to their ability to fabricate geometrically complex components directly from digital models in a layer-by-layer manner (DebRoy et al., 2018; Frazier, 2014).Powder bed fusion (PBF) methods stand out among these technologies for dimensional accuracy and microstructure control; however, the high equipment and operating costs of laser- and electron-beam-based systems limit their adoption by small and medium-sized enterprises and research institutions (Frazier, 2014; Dejene and Lemu, 2023).

Powder bed arc additive manufacturing (PBAAM) has attracted growing interest as a low-cost alternative in which a tungsten inert gas (TIG) arc replaces the laser or electron beam (Moreira et al., 2020; Dong et al., 2021). Three primary control variables govern single-track formation: electrode diameter φ (mm), welding current I (A), and travel speed v (mm/s) (Lancaster, 1987). The combination of these three variables jointly determines single-track morphology, track continuity and width uniformity (Moreira et al., 2020; Dong et al., 2021).

Continuous and stable single-track formation is the fundamental prerequisite for reliable multi-layer PBAAM fabrication. Process instabilities at the single-track level, including balling, lack of fusion and porosity, propagate cumulatively into subsequent layers (Yadroitsev et al., 2007; Li et al., 2012). Systematic single-track investigations are an integral part of process window development for any PBF variant (Katagiri et al., 2023; Wang et al., 2023). Previous PBAAM studies have examined the effects of I, v and layer thickness on single-track morphology (Çelikel and Balci, 2026). Balcı and Alibeyoglu (2026) demonstrated that the inclined-bed experimental approach enables efficient identification of continuity thresholds as a function of layer thickness within a single campaign.

Two key metrics are used to quantify single-track morphology. The maximum gap length L_{gap} (mm), measured by sliding-window analysis of the binary image, serves as an objective indicator of track continuity. The coefficient of variation of width $CV = \sigma_w/\bar{w}$ provides a normalised descriptor of geometric uniformity, where $\bar{w}$

(mm) is the mean track width and σ_w (mm) is its standard deviation. Image-based analysis methods enable objective and reproducible measurement of both metrics (Martucci et al., 2021). Çelikel and Balcı (2026) established an image classification framework based on Otsu thresholding with expert manual correction on the same PBAAM system and demonstrated high agreement with expert visual labels.

Electrode diameter φ is a critical parameter distinguishing TIG-based PBAAM from other PBF processes. Decreasing φ concentrates the arc into a narrower footprint, increasing local energy density per unit current; increasing φ broadens the arc profile and distributes energy more homogeneously (Kou, 2003; Lancaster, 1987). Despite this direct physical influence on the process window, φ has not been systematically investigated as an independent variable in PBAAM. In the prior study by Balcı and Alibeyoğlu (2026) φ = 1.6 mm was selected based on qualitative observation without a systematic quantitative comparison, representing a clear research gap that the present study addresses.

The specific novelty of this work is that electrode diameter is treated as an independent process variable in TIG-based PBAAM for the first time within a full-factorial single-track framework. Unlike previous studies in which electrode diameter was selected qualitatively or kept constant, the present study quantitatively links φ to track width, continuity, width uniformity and process-window boundaries. Therefore, the study provides a directly applicable electrode-diameter selection criterion for inclined-bed PBAAM of 316L stainless steel.

2. Materials and Methods

2.1. Experimental System and Powder Material

All experiments were conducted using the custom-built PBAAM system described in detail in previous studies (Balcı and Alibeyoglu, 2026; Çelikel and Balci, 2026) at Kafkas University Department of Mechanical Engineering. The system comprises a TIG power source and a three-axis ($X - Y - Z$) stepper-motor motion platform. High-purity argon shielding gas was supplied at a constant flow rate of 6 L/min through a gas lens. The electrode-to-powder-bed stand-off distance was fixed at L = 0.5 mm, a critical dimension affecting arc ignition stability that was determined through systematic screening experiments by Çelikel and Balci (2026)(Figure 1).

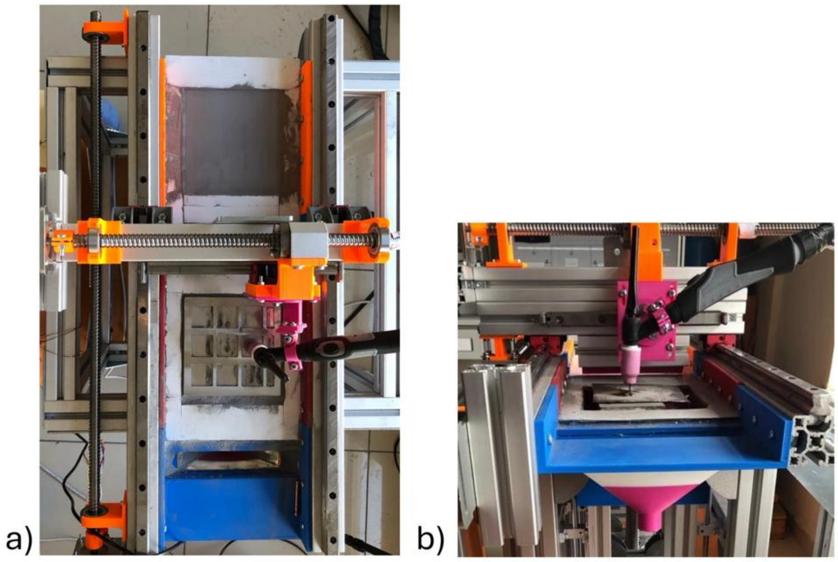

Figure 1. Schematic representation of the PBAAM experimental setup: a) top view; b) front view.

Gas-atomised 316L stainless steel powder was used as feedstock with particle size range 15–53 µm (D10: 18.7 µm; D50: 31.1 µm; D90: 51.7 µm). Chemical composition (wt.%): Cr 16.83; Ni 10.93; Mo 2.27; Mn 0.67; Si 0.66; C 0.008; P 0.033; S 0.005; Fe balance. Substrate plates (316L SS, 2 mm thick, 10 × 140 mm) were ground and ultrasonically cleaned prior to each experiment.

2.2. Electrode Diameters and Experimental Matrix

Lanthanated tungsten electrodes (2% La_2O_3) were evaluated at three diameters of 0.6, 0.8 and 1.0 mm. For each electrode diameter, three current levels of 20, 25 and 30 A and three travel speeds of 2, 3 and 4 mm/s were applied in a full-factorial design, yielding 27 parameter combinations in total. The current range was restricted to 20–30 A, as continuous melting cannot be sustained below 20 A and melt pool expansion becomes uncontrolled above 30 A (Çelikel and Balci, 2026). Travel speed was bounded between 2 and 4 mm/s, since severe discontinuities emerge at all electrode diameters above 4 mm/s (Balcı and Alibeyoglu, 2026). Each combination was tested once. This single-repetition design is acknowledged as a limitation of the experimental campaign. However, the objective of the present work was process-window screening rather than formal repeatability quantification. In addition, each single track was evaluated over the full calibrated active region, providing a large number of spatial width measurements along the scan direction. The use of Otsu thresholding, expert manual correction and sliding-window metrics therefore supports internally consistent comparison among the 27 parameter combinations. Future work will include repeated trials to quantify experimental uncertainty. The detailed experimental matrix is presented in Table 1.

Table 1. Full-factorial experimental matrix (3^3 = 27 combinations). φ: electrode diameter (mm); I: welding current (A); v: travel speed (mm/s)

φ (mm)	I (A)	v (mm/s)
0.6	20 / 25 / 30	2 / 3 / 4
0.8	20 / 25 / 30	2 / 3 / 4
1.0	20 / 25 / 30	2 / 3 / 4

2.3. Inclined-Bed Setup and Image Calibration

One end of the substrate plate was elevated to create a linearly varying powder layer thickness profile (Figure 2), described by equation 1;

$$t(x) = 0.4 \times (x/140)\ [mm] \quad (1)$$

where x (mm) denotes position along the scan direction and t(x) (mm) denotes local powder layer thickness (equation 1). The thickness increases from approximately zero at x = 0 to 0.40 mm at x = 140 mm. This approach enables data collection across a wide thickness range within a single experimental campaign, facilitating identification of parameter-specific critical thickness thresholds (Balcı and Alibeyoglu, 2026). After each experiment, the solidified track was imaged from above using a Sony Mark 5 camera with an ND filter (ISO 80, f/2.8, 1/12,000 s), and the horizontal resolution was calibrated to 87.2 μm/pixel using known substrate dimensions.

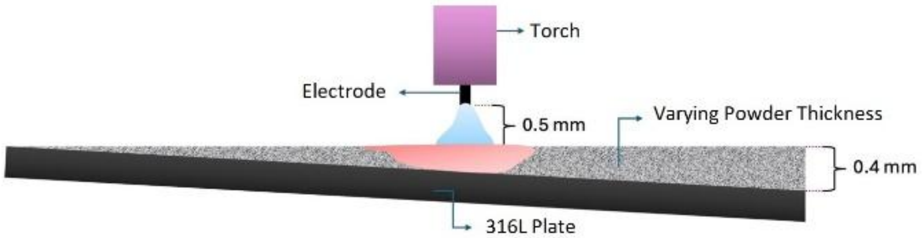

Figure 2. Schematic representation of the inclined-bed setup.

2.4. Image Processing and Two-Stage Classification Framework

The image processing pipeline comprises five sequential steps. First, the raw top-view image is converted to greyscale. Second, Otsu global thresholding is applied, where white pixels represent solidified material and black pixels represent material absence (Otsu, 1979). Third, expert manual correction is applied where automated thresholding fails to accurately delineate melt boundaries, an approach validated by Çelikel and Balci on the same system (Çelikel and Balci, 2026). Fourth, the active melting region is identified from the first white-pixel column at position x_{start} (mm) to the last white-pixel column at x_{end} (mm), giving an active region length of $L_{active} = x_{end} - x_{start}$ (mm). Fifth, track width $w(x)$ (mm) is measured by transverse binary projection at each position x within the active region.

A sliding window of *±15* mm is applied at each x. The longest continuous zero-width sequence within the window is recorded as the local maximum gap length $L_{gap}(x)$ (mm). Mean width $\bar{w}$ (mm), standard deviation σ_W (mm) and coefficient of variation CV are computed as (Montgomery, 2017) (equations 2-4):

$$\bar{w} = (1/n) \cdot \sum_i w(x_i) \quad (2)$$

$$\sigma_w = \sqrt{\left[\left(\frac{1}{n-1}\right) \cdot \sum_i (w(x_i) - \bar{w})^2\right]} \quad (3)$$

$$CV = \sigma_w / w \quad (4)$$

where n is the total column count in the active region. The two-stage classification rule is applied independently at each x; $L_{threshold}$ (mm) and $CV_{threshold}$ are the gap and CV thresholds, respectively (equations 5-7):

$$L_{gap}(x) > L_{threshold} \rightarrow \text{"Fragmented / Balling"} \quad (5)$$

$$L_{gap}(x) \leq L_{threshold}\ and\ CV > CV_{threshold} \rightarrow \text{"}Continuous - Unstable\text{"} \quad (6)$$

$$L_{gap}(x) \leq L_{threshold}\ and\ CV \leq CV_{threshold} \rightarrow \text{"}Continuous - Stable\text{"} \quad (7)$$

Independent application at each x enables zone-wise regime detection within a single track; regime boundaries are reported in terms of $t(x)$. All computations were performed in Python 3 (Pedregosa et al., 2011).

2.5. Threshold Sensitivity Analysis and Scenario Selection

To systematically evaluate the sensitivity of classification outcomes to threshold selection, six scenarios (S1–S6) were constructed by combining two gap threshold values of 0.09 and 0.50 mm with three CV threshold values of 0.12, 0.15 and 0.20, and applied to all 27 combinations (Table 2). Each scenario was evaluated independently without a priori preference, with scenario selection deferred to the Results section based on comparative data. The threshold values were derived from literature. A gap threshold of 0.09 mm represents the minimum gap criterion reported in laser PBF studies, while 0.50 mm corresponds to approximately 15–25% of the mean track width at arc scale (Balcı and Alibeyoglu, 2026). A *CV* threshold of 0.12 follows laser PBF standards (Martucci et al., 2021), and 0.20 reflects the upper bound reported for DED and arc-based systems (Sampson et al., 2020).

Table 2. Threshold sensitivity analysis scenarios

Sn.	L_{gap}	CV (mm/s)	Source
S1	0.09	0.12	(Martucci et al., 2021)
S2	0.09	0.15	(Çelikel and Balci, 2026)
S3	0.09	0.20	(Sampson et al., 2020)
S4	0.50	0.12	(Balcı and Alibeyoglu, 2026)
S5 ★	0.50	0.15	(Çelikel and Balci, 2026)
S6	0.5	0.2	(Sampson et al., 2020)

★ = combination selected in the results section.

2.6. Process Map and Linear Regression Models

Two complementary analyses were performed. (i) Process map: regime labels assigned to each $\varphi - I - v$ combination were visualized as a colour-coded matrix, making process window boundaries directly visible (Schwerz and Nyborg, 2021; Scipioni Bertoli et al., 2017) and identifying which parameter disrupts continuity under which conditions — an approach widely used in WAAM literature (Raut and Taiwade, 2021; Williams et al., 2016). (ii) Multiple linear regression: two models were fitted with φ (mm), I (A) and v (mm/s) as independent variables and w̄ (mm) and CV as separate responses (equations 8 and 9):

$$\overline{w} = \beta_0 + \beta_\varphi \cdot \varphi + \beta_I \cdot I + \beta_v \cdot v \quad (8)$$

$$CV = \gamma_0 + \gamma_\varphi \cdot \varphi + \gamma_I \cdot I + \gamma_v \cdot v \quad (9)$$

where β_0 and γ_0 are intercepts; β_φ, β_I, β_v and γ_φ, γ_I, γ_v are regression coefficients for φ, I and v on $\bar{w}$ and CV, respectively. Model fit was assessed by R^2 and coefficient significance by t-test (α = 0.05) (Montgomery, 2017). All computations were performed in Python 3 (Pedregosa et al., 2011).

3. Results

3.1. Binary Image Analysis and Active Region Detection

All 27 combinations were successfully binarized using Otsu thresholding with expert manual correction where required. Active region start x_{start} ranged from 0.4 to 7.0 mm and end x_{end} from 120 to 133 mm across all combinations. Small x_{start} values confirm that melting begins immediately after arc ignition in the thin powder region (t ≈ 0); x_{end} values consistently below 140 mm reflect exhaustion of melting capacity in the thick powder region. Binary images and sliding-window local regime profiles for each electrode diameter are presented in Figures 3–5, with horizontal axes scaled in x (mm) and $t(x)$ (mm). Coloured bands indicate Stable (green), Unstable (yellow) and Fragmented (red) zones.

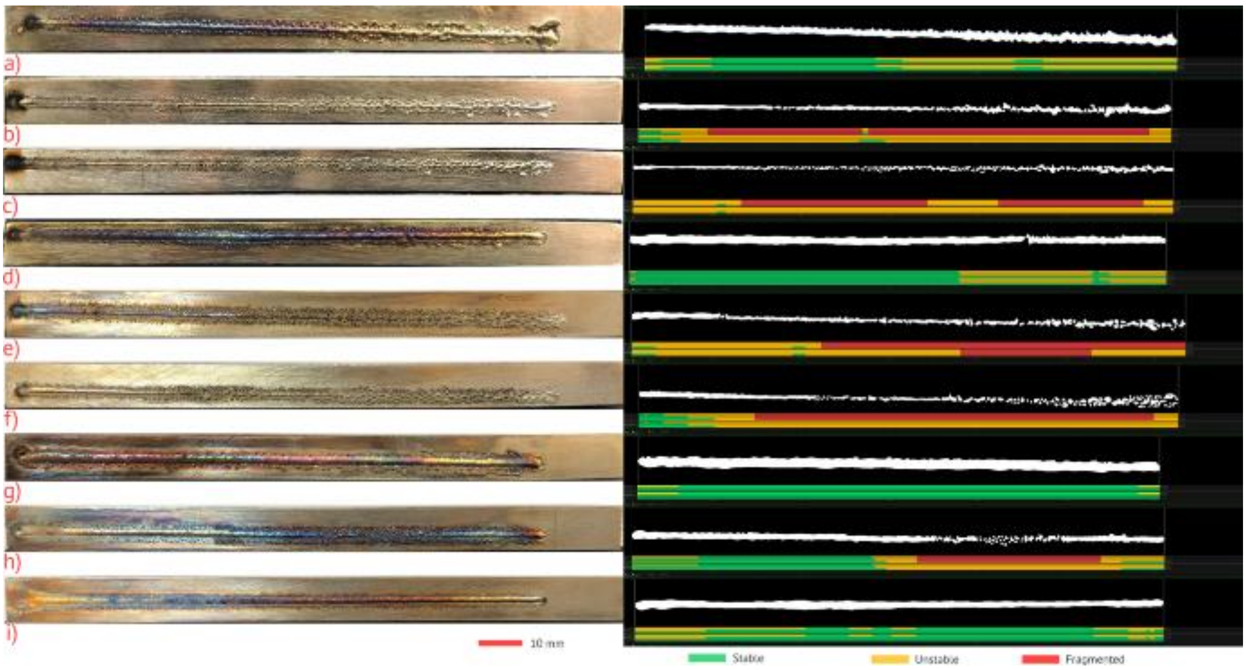

Figure 3. Single-track morphology images and local regime profiles presented vertically for six threshold scenarios (S1–S6) obtained under inclined-bed conditions at different current and travel speed parameters for electrode diameter φ = 0.6 mm: a) I = 20 A, v = 2 mm/s; b) I = 20 A, v = 3 mm/s; c) I = 20 A, v = 4 mm/s; d) I = 25 A, v = 2 mm/s; e) I = 25 A, v = 3 mm/s; f) I = 25 A, v = 4 mm/s; g) I = 30 A, v = 2 mm/s; h) I = 30 A, v = 3 mm/s; i) I = 30 A, v = 4 mm/s.

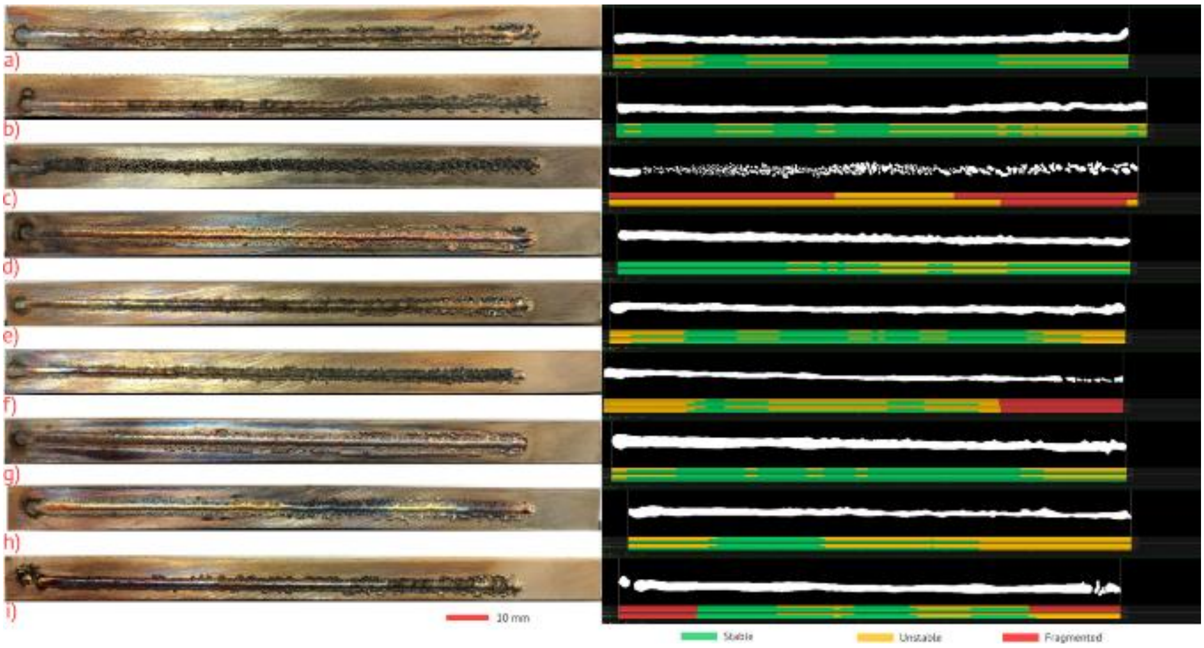

Figure 4. Single-track morphology images and local regime profiles presented vertically for six threshold scenarios (S1–S6) obtained under inclined-bed conditions at different current and travel speed parameters for electrode diameter φ = 0.8 mm: a) I = 20 A, v = 2 mm/s; b) I = 20 A, v = 3 mm/s; c) I = 20 A, v = 4 mm/s; d) I = 25 A, v = 2 mm/s; e) I = 25 A, v = 3 mm/s; f) I = 25 A, v = 4 mm/s; g) I = 30 A, v = 2 mm/s; h) I = 30 A, v = 3 mm/s; i) I = 30 A, v = 4 mm/s.

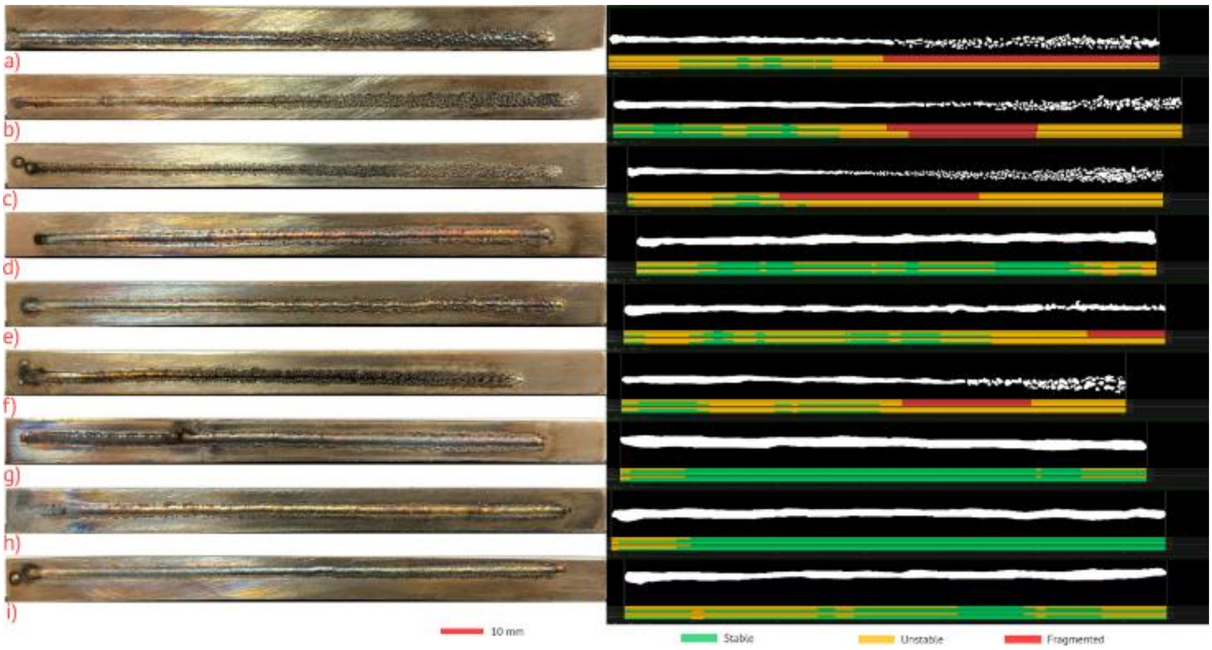

Figure 5. Single-track morphology images and local regime profiles presented vertically for six threshold scenarios (S1–S6) obtained under inclined-bed conditions at different current and travel speed parameters for electrode diameter φ = 1.0 mm: a) I = 20 A, v = 2 mm/s; b) I = 20 A, v = 3 mm/s; c) I = 20 A, v = 4 mm/s; d) I = 25 A, v = 2 mm/s; e) I = 25 A, v = 3 mm/s; f) I = 25 A, v = 4 mm/s; g) I = 30 A, v = 2 mm/s; h) I = 30 A, v = 3 mm/s; i) I = 30 A, v = 4 mm/s.

3.2. Six-Scenario Comparison and Scenario Selection

The Stable, Unstable and Fragmented distributions obtained by applying S1–S6 to all 27 combinations are summarised in Table 3. Scenarios S1 and S2, both using a gap threshold of 0.09 mm, classify 13 combinations as Fragmented. This outcome arises because gaps of approximately 0.09 mm, equivalent to one pixel, can originate from image noise or partial fusion zones and do not represent genuine physical discontinuity. Scenario S3, which combines the same gap threshold with a CV threshold of 0.20, produces 13 Stable classifications. A CV threshold of 0.20 assigns a Stable label to tracks with CV values as high as 0.267, which exhibit clearly irregular width profiles on visual inspection and cannot be considered geometrically stable. Scenario S4, using a CV threshold of 0.12, yields only one Stable combination, as this value was calibrated for laser PBF systems and is systematically exceeded by the wider and more dynamic arc melt pool. Scenario S6 contains the same physical inconsistencies as S3.

Scenario S5, combining a gap threshold of 0.50 mm with a CV threshold of 0.15, is the only physically defensible combination. A gap threshold of 0.50 mm corresponds to 15–25% of the mean track width at arc scale and is directly adopted by Balcı and Alibeyoğlu (2026) and Çelikel and Balcı (2026) . A CV threshold of 0.15 is less strict than the laser PBF lower bound of 0.12 yet stricter than the DED and arc-based upper bound of 0.20, reflecting the more dynamic nature of arc melt pools (Kou, 2003; Lancaster, 1987), and was validated on the same system by Çelikel and Balcı (2026). All subsequent analyses are based on S5 labels.

The suitability of S5 arises from the combined use of a physically meaningful gap threshold and a moderate width-uniformity threshold. The 0.50 mm gap threshold avoids classifying one-pixel image artefacts as true discontinuities, while CV_{th} = 0.15 is sufficiently strict to reject visibly irregular arc tracks but not as restrictive as laser-PBF-based criteria. Thus, S5 simultaneously captures continuity and geometric uniformity at the millimetre-scale melt-pool width typical of TIG-based PBAAM.

Table 3. Distribution of Continuous-Stable, Continuous-Unstable and Fragmented/Balling classifications for S1–S6 across all 27 combinations and selection justification

Sc.	L_{gap} threshold (mm)	$CV_{threshold}$	Stable	Unstable	Fragmented	Note
S1	0.09	0.12	1	13	13	Noise-sensitive
S2	0.09	0.15	3	11	13	Noise-sensitive
S3	0.09	0.20	13	1	13	CV too loose
S4	0.50	0.12	1	21	5	CV too strict
S5 ★	0.50	0.15	3	19	5	Physical + lit.
S6	0.50	0.20	13	9	5	CV too loose

★ = combination selected in the results section.

3.3. Regime Classification with S5 Labels and Electrode-Based Assessment

Under S5, 3 out of 27 combinations are classified as Continuous-Stable (CV ≤ 0.15, L_{gap} =0), 19 as Continuous-Unstable and 5 as Fragmented/Balling. The CV, L_gap and w̄ values together with regime labels for all 27 combinations are given in Table 4, and electrode-based summary metrics are presented in Table 5.

For φ = 0.6 mm, Fragmented/Balling was observed only at I = 25 A and v = 3 mm/s (L_{gap} = 0.61 mm). All combinations at I = 30 A produced continuous tracks, with the lowest width variability recorded at I = 30 A and v = 2 mm/s (CV = 0.096). Mean track width and mean CV for continuous tracks were 1.35 mm and 0.282, respectively.

For φ = 0.8 mm, Fragmented/Balling was confined exclusively to v = 4 mm/s across all three current levels. At v = 2 and 3 mm/s, continuous tracks were obtained at all current levels including I = 20 A. The mean CV of 0.184 for continuous tracks is approximately 35% lower than the corresponding values for the other two electrode diameters, representing a meaningful advantage in width uniformity. Mean track width was 1.72 mm.

For φ = 1.0 mm, the fewest Fragmented occurrences (1 out of 9) and the highest Stable count (2 out of 9, both at I = 30 A) were obtained. However, at I = 20 A, CV values ranged from 0.381 to 0.549, representing the highest instability observed across all 27 combinations. Mean CV and mean track width for continuous tracks were 0.281 and 1.64 mm, respectively.

3.4. Process Map and the Decisive Role of Travel Speed

The process map reveals travel speed v as the most critical parameter governing the process window (Table 6). At v = 2 mm/s, all 9 combinations (100%) produced continuous tracks across every φ and I level, with stable tracks at every I = 30 A condition (3/3). At v = 3 mm/s, 7/9 (78%) remained continuous; Fragmented behaviour emerged at φ = 0.6 mm · 25 A and φ = 1.0 mm · 20 A, and stability at I = 30 A dropped to 2/3. At v = 4 mm/s, only 5/9 (56%) were continuous, all four Fragmented occurrences concentrated at φ = 0.8 mm, and no stable tracks remained at I = 30 A (0/3). The monotonic collapse of the I = 30 A stability margin (3/3 → 2/3 → 0/3) confirms that increasing v erodes the process window even at the most favourable current setting.

Table 4. Classification of all 27 combinations with S5 labels. CV: coefficient of variation ($\sigma_w/\bar{w}$); L_{gap} : maximum gap length (mm); w̄: mean track width (mm)

φ (mm)	I (A)	v (mm/s)	L_{gap} (mm)	w̄ (mm)	Regime
0.6	20	2	0.00	1.66	Continuous-Unstable
0.6	20	3	0.35	0.93	Continuous-Unstable
0.6	20	4	0.35	0.65	Continuous-Unstable
0.6	25	2	0.00	1.61	Continuous-Unstable
0.6	25	3	0.61	—	Fragmented-Balling
0.6	25	4	0.44	0.97	Continuous-Unstable
0.6	30	2	0.00	2.18	Continuous - Stable
0.6	30	3	0.26	1.24	Continuous-Unstable
0.6	30	4	0.00	1.54	Continuous-Unstable
0.8	20	2	0.00	1.67	Continuous-Unstable
0.8	20	3	0.00	1.58	Continuous-Unstable
0.8	20	4	0.52	—	Fragmented-Balling
0.8	25	2	0.00	1.75	Continuous-Unstable
0.8	25	3	0.00	1.60	Continuous-Unstable
0.8	25	4	0.61	—	Fragmented-Balling
0.8	30	2	0.00	2.19	Continuous-Unstable
0.8	30	3	0.00	1.52	Continuous-Unstable
0.8	30	4	0.96	—	Fragmented-Balling
1.0	20	2	0.44	1.33	Continuous-Unstable
1.0	20	3	0.52	—	Fragmented-Balling
1.0	20	4	0.26	1.31	Continuous-Unstable
1.0	25	2	0.00	1.83	Continuous-Unstable
1.0	25	3	0.17	1.34	Continuous-Unstable
1.0	25	4	0.26	1.44	Continuous-Unstable
1.0	30	2	0.00	2.19	Continuous-Stable
1.0	30	3	0.00	1.90	Continuous-Stable
1.0	30	4	0.00	1.80	Continuous-Unstable

Table 5. Summary metrics by electrode diameter under S5 labels considering continuous tracks only

φ (mm)	Continuous-Stable	Continuous-Unstable	Fragmented-Balling	$\bar{w}_{avg}$ (mm)	CV_{avg}	Min. CV
0.6	1/9	7/9	1/9	1.35	0.282	0.096
0.8	0/9	5/9	4/9	1.72	0.184	0.157
1.0	2/9	6/9	1/9	1.64	0.281	0.134

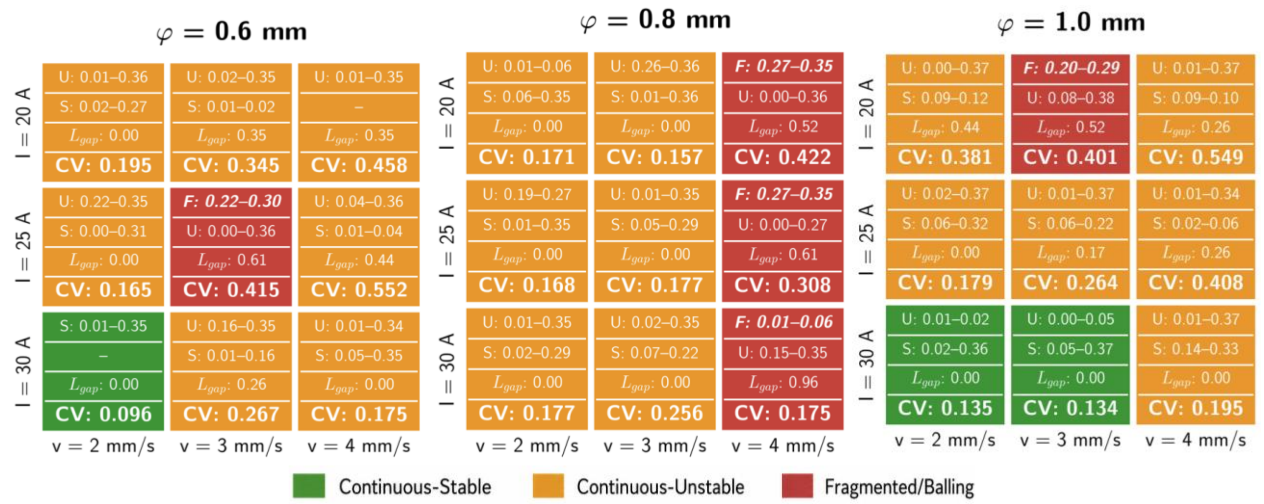

Figure 6. Process map: regime label under S5 (Continuous -Stable = green, Continuous -Unstable = yellow, Fragmented-Balling = red) for each φ × I × v combination. Rows: v; columns: I; panels: φ.

Table 6. Continuity summary by travel speed and Continuous-Stable combination counts at I = 30 A

v (mm/s)	Continuous tracks	Fragmented-Balling	% Continuous	Continuous-Stable at I = 30 A
2	9/9	0/9	100%	3/3
3	7/9	2/9	78%	2/3
4	5/9	4/9	56%	0/3

3.5. Regression Model Results

The width regression model expresses mean track width w̄ (mm) as a function of electrode diameter φ (mm), welding current I (A) and travel speed v (mm/s) (equation 10):

$$\bar{w} = 0.354 + 0.762.\varphi + 0.05.I - 0.233.v\ [mm] \qquad (10)$$

The model achieves R^2 = 0.626, indicating that 62.6% of the variance in w̄ is explained by the three parameters. All coefficients are statistically significant at $\alpha = 0.05$: $\varphi\ (\beta = 0.762, p = 0.019)$, $I\ (\beta = 0.050, \mathrm{P} < 0.001)$ and $v\ (\beta = -0.233, p < 0.001)$ (Table 7). Increasing electrode diameter and current widens the track, while increasing travel speed narrows it, consistent with findings reported in WAAM (Raut and Taiwade, 2021; Williams et al., 2016) and LPBF literature (Z. Dong et al., 2019).

The CV regression model is expressed as (equation 11):

$$CV = 0.421 - 0.006.\varphi - 0.016.I + 0.088.v \qquad (11)$$

The model yields R^2 = 0.562. Welding current (γ = −0.016, P=0.001) and travel speed (γ = 0.088, P<0.001) are statistically significant, whereas the electrode diameter coefficient is not (γ = −0.006, P=0.955). This constitutes a critical finding: although electrode diameter significantly affects mean track width (β_φ = 0.762, P=0.019), it does not linearly influence width uniformity as measured by CV. The linear component of CV is governed primarily by welding current and travel speed.

Table 7. Multiple linear regression results

Model	Response variable	β_φ / γ_φ	β_I / γ_I	β_v / γ_v	R^2	Significant factors
w̄	w̄ (mm)	0.762*	0.050***	−0.233***	0.626	φ, I, v
CV	CV (−)	−0.006 (ns)	−0.016***	0.088***	0.562	I, v (φ ns)

*P<0.05; ***P<0.001; ns= not significant

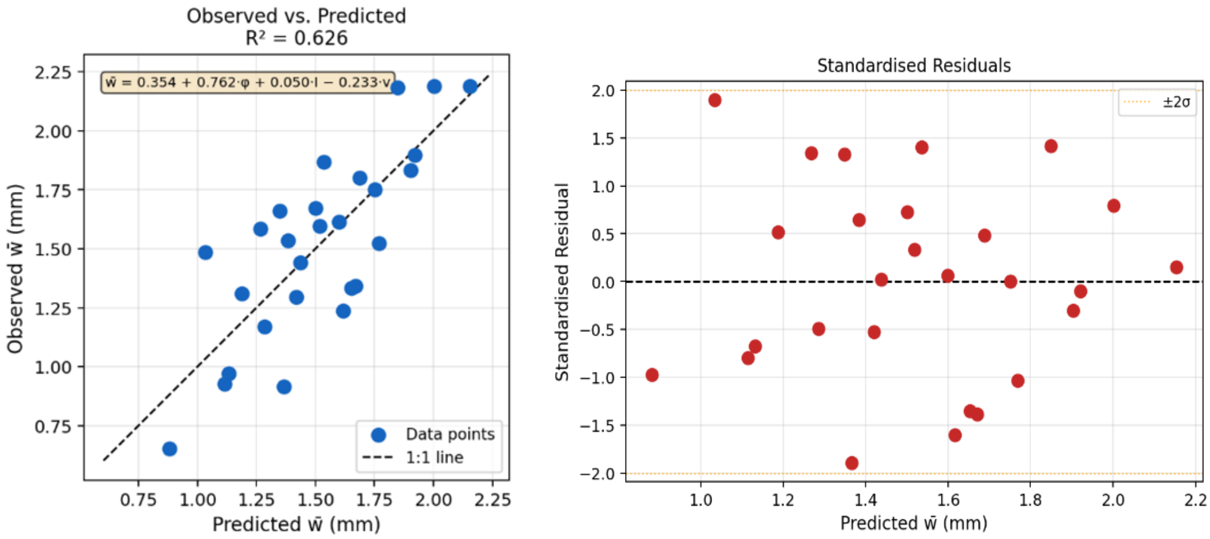

Figure 7. Observed vs. model-predicted w̄ values (R^2 = 0.626) and standardised residuals.

4. Discussion

4.1. Methodological Importance of Threshold Selection

The six-scenario comparison demonstrates that scenarios S1 and S2, both employing a gap threshold of 0.09 mm, are excessively sensitive to noise. Gaps of this magnitude, equivalent to approximately one pixel, can arise from image noise or partial fusion zones and do not represent genuine physical discontinuity. Scenarios S3 and S6, which use a CV threshold of 0.20, assign a Stable label to tracks with CV values as high as 0.267. Although Sampson et al. report values up to 0.20 for DED systems, tracks at this CV level in the present study exhibit clearly irregular width profiles on visual inspection and cannot be considered geometrically stable (Sampson et al., 2020). Scenario S4, with a CV threshold of 0.12, was calibrated for laser PBF systems and is systematically exceeded by the wider and more dynamic arc melt pool (Lancaster, 1987). Scenario S5, combining a gap threshold of 0.50 mm with a CV threshold of 0.15, is the only combination consistent with the physical characteristics of this system. A gap threshold of 0.50 mm corresponds to 15–25% of the mean track width at arc scale and is directly adopted by Balcı and Alibeyoğlu (2026) and Çelikel and Balcı (2026). Therefore, the selected S5 criterion should not be interpreted as a relaxation of laser-PBF standards, but as a scale-adjusted criterion for the wider, more dynamic and millimetre-scale melt pools generated by TIG-based PBAAM.

4.2. Effect of Electrode Diameter on Track Width and Continuity

The regression analysis demonstrates that φ exerts a statistically significant positive effect on w̄ (β_φ = 0.762, P=0.019) but no significant linear effect on *CV* (P=0.955). This joint interpretation provides a critical physical insight: electrode diameter determines melt pool width but does not linearly control width uniformity. This is consistent with TIG arc physics: increasing φ broadens the arc footprint and reduces local energy density at constant current (Kou, 2003; Lancaster, 1987); the result is a wider but not necessarily more uniform track. Consequently, φ acts as a track size determinant rather than a linear uniformity controller.

Nevertheless, the process map reveals that φ structurally shapes the process window. For φ = 0.8 mm, all Fragmented combinations were confined to v = 4 mm/s; continuity was maintained at all current levels including I = 20 A at v = 2 and 3 mm/s. For φ = 0.6 mm, *CV* > 0.195 at I = 20 A across all travel speeds indicates that low current is insufficient for this small electrode. For φ = 1.0 mm, CV = 0.381–0.549 at I = 20 A shows that the enlarged arc footprint reduces energy density below the critical threshold at low current (Kou, 2003; Lancaster, 1987). At both extremes, I = 30 A becomes necessary to achieve continuity and stability.

4.3. Roles of Travel Speed and Current

The regression model identifies v as the most statistically decisive parameter for both w̄ (β_v = −0.233, P<0.001) and CV (γ_v = 0.088, P<0.001). Increasing v simultaneously narrows the track and increases width variability because the arc-powder interaction time decreases and the melt pool becomes undersized, activating the balling mechanism (Li et al., 2012; Yadroitsev et al., 2007). The process map corroborates this: 100% continuous tracks at v = 2 mm/s vs. four Fragmented occurrences at v = 4 mm/s. The protective role of low travel speed across all electrode diameters and current levels suggests that a travel speed ceiling should be treated as a primary constraint in PBAAM process window design — consistent with WAAM (Raut and Taiwade, 2021; Williams et al., 2016) and LPBF (Dong et al., 2019; Wang et al., 2023) literature. Current *I* exert a significant positive effect on w̄ (β_I = 0.050, *P<0.001*) and a significant negative effect on CV (γ_I = −0.016, P=0.001): all three Stable combinations were obtained at *I* = 30 A.

4.4. Powder Thickness and Local Regime Transition

The sliding window analysis reveals a systematic three-zone behaviour for all electrode diameters: Stable or near-Stable in the thin powder zone (t < 0.10 mm); Unstable in the intermediate zone (0.10 < t < 0.25 mm);

Fragmented/Balling tendency in the thick powder zone (t > 0.25 mm). This pattern is consistent with the critical layer thickness findings of Balcı and Alibeyoğlu (2026). The critical thickness threshold t_{crit} the t value at which L_{gap} first exceeds 0.50 mm — varies with φ and I. The earliest discontinuity was at φ = 0.6 mm·25A·3mm/s (t_{crit} ≈ 0.22 mm); continuity was maintained below t < 0.37 mm for φ = 1.0 mm·30 A combinations. Large φ combined with high I can melt thicker powder layers over a broader arc footprint, while small φ at moderate current may develop excessive local energy density that destabilises the arc in thick powder regions (Kou, 2003; Lancaster, 1987).

4.5. Limitations and Future Work

This study is limited to single-track level; multi-track and multi-layer behaviour were not investigated. Each combination was tested once; repeated experiments would enable quantitative uncertainty assessment. The linear regression models (R^2 = 0.562–0.626) offer moderate explanatory power; φ × I and φ × v interaction terms could increase this. The manual correction step introduces a subjective component. Future studies could extend to φ = 1.6 mm for a unified four-diameter process map, conduct multi-layer PBAAM experiments to test scalability of single-track findings, and evaluate generalisability across different powder materials such as Ti6Al4V and Inconel 625. Although repeated experiments were not performed, the image-based analysis generated spatially resolved width and continuity data along each track, which enabled consistent within-track and between-parameter comparison. Nevertheless, the absence of repetitions prevents direct estimation of experimental scatter, and this should be addressed in future repeatability studies.

5. Conclusions

The effect of electrode diameter (φ = 0.6, 0.8 and 1.0 mm) on single-track morphology and process window in inclined-bed PBAAM of 316L stainless steel powder was systematically investigated using Otsu-based image analysis with manual correction, six-scenario threshold analysis, a process map and multiple linear regression. The following conclusions are drawn.

Six threshold scenarios were applied to all 27 combinations and compared. A gap threshold of 0.09 mm was found to be excessively sensitive to image noise, while a CV threshold of 0.20 produced physically inconsistent Stable classifications. Scenario S5 ($L_{threshold}$ = 0.50 mm, $CV_{threshold}$ = 0.15) was identified as the only combination consistent with the physical characteristics of the arc system and methodologically continuous with prior studies.

Process map analysis identified travel speed as the most critical parameter governing the process window. At v = 2 mm/s, all nine combinations produced continuous tracks, whereas at v = 4 mm/s only five out of nine were continuous and four Fragmented occurrences were observed. The width regression model (R^2 = 0.626) showed that electrode diameter (β = 0.762, P=0.019), welding current (β = 0.050, P<0.001) and travel speed (β = −0.233, P<0.001) all significantly affect track width. Increasing electrode diameter and current widens the track, while increasing travel speed narrows it.

The CV regression model (R^2 = 0.562) revealed that electrode diameter has no significant linear effect on width uniformity (P=0.955). Width variability is primarily governed by welding current (γ = −0.016, P=0.001) and travel speed (γ = 0.088, P<0.001), establishing electrode diameter as a track size determinant rather than a uniformity controller.

The φ = 0.8 mm electrode confined all Fragmented combinations to v = 4 mm/s only and produced continuous tracks at all current levels including I = 20 A at v = 2 and 3 mm/s. The mean CV of 0.184 for continuous tracks was approximately 35% lower than the values obtained for φ = 0.6 mm (0.282) and φ = 1.0 mm (0.281), indicating the widest and most balanced process window among the three electrode diameters studied.

Author Contributions

The percentages of the authors' contributions are presented below. All authors reviewed and approved the final version of the manuscript.

	A.B.	F.A.
C	60	40
D	50	50
S	70	30
DCP	50	50
DAI	50	50
L	50	50
W	50	50
CR	50	50
SR	20	80
PM	70	30
FA	100	0

C= concept, D= design, S= supervision, DCP= data collection and/or processing, DAI= data analysis and/or interpretation, L= literature search, W= writing, CR= critical review, SR= submission and revision, PM= project management, FA= funding acquisition.

Conflict of Interest

The authors declared that there is no conflict of interest.

Ethical Consideration

Ethics committee approval was not required for this study because of there was no study on animals or humans.

Acknowledgements

This study was supported by the Scientific Research Projects Coordination Unit of Kafkas University under project number 2023-FM-40. The authors gratefully acknowledge this financial support.

References

Balcı, A., & Alibeyoglu, F. (2026). Effect of layer thickness and scanning parameters on melt pool geometry and track continuity in powder-bed arc additive manufacturing. *Metals*, *16*(3), Article 259. https://doi.org/10.3390/met16030259

Çelikel, O. E., & Balcı, A. (2026). Interpretable machine learning for process parameter analysis in arc-driven powder bed fusion of 316L stainless steel. *Mathematics*, *14*(8), Article 1296. https://doi.org/10.3390/math14081296

DebRoy, T., Wei, H. L., Zuback, J. S., Mukherjee, T., Elmer, J. W., Milewski, J. O., Beese, A. M., Wilson-Heid, A., De, A., & Zhang, W. (2018). Additive manufacturing of metallic components – Process, structure and properties. *Progress in Materials Science*, *92*, 112–224. https://doi.org/10.1016/j.pmatsci.2017.10.001

Dejene, N. D., & Lemu, H. G. (2023). Current status and challenges of powder bed fusion-based metal additive manufacturing: Literature review. *Metals*, *13*(2), Article 424. https://doi.org/10.3390/met13020424

Dong, B., Wang, Z., Pan, Z., Muránsky, O., Shen, C., Reid, M., Wu, B., Chen, X., & Li, H. (2021). On the development of pseudo-eutectic AlCoCrFeNi2.1 high entropy alloy using Powder-bed Arc Additive Manufacturing (PAAM) process. *Materials Science and Engineering: A*, *802*, Article 140639. https://doi.org/10.1016/j.msea.2020.140639

Dong, Z., Liu, Y., Wen, W., Ge, J., & Liang, J. (2019). Effect of hatch spacing on melt pool and as-built quality during selective laser melting of stainless steel: Modeling and experimental approaches. *Materials*, *12*(1), Article 50. https://doi.org/10.3390/ma12010050

Frazier, W. E. (2014). Metal additive manufacturing: A review. *Journal of Materials Engineering and Performance*, *23*(6), 1917–1928. https://doi.org/10.1007/s11665-014-0958-z

Katagiri, J., Kusano, M., Minamoto, S., Kitano, H., Daimaru, K., Tsujii, M., & Watanabe, M. (2023). Melt pool shape evaluation by single-track experiments and finite-element thermal analysis: Balling and lack of fusion criteria for generating process window of Inconel738LC. *Materials*, *16*(4), Article 1729. https://doi.org/10.3390/ma16041729

Kou, S. (2003). *Welding metallurgy* (2nd ed.). Wiley-Interscience.

Lancaster, J. F. (1987). The physics of fusion welding. Part 1: The electric arc in welding. *IEE Proceedings B (Electric Power Applications)*, *134*(5), 233–254. https://doi.org/10.1049/ip-b.1987.0040

Li, R., Liu, J., Shi, Y., Wang, L., & Jiang, W. (2012). Balling behavior of stainless steel and nickel powder during selective laser melting process. *The International Journal of Advanced Manufacturing Technology*, *59*(9), 1025–1035. https://doi.org/10.1007/s00170-011-3566-1

Martucci, A., Marinucci, F., Sivo, A., Aversa, A., Manfredi, D., Bondioli, F., Fino, P., & Lombardi, M. (2021). An automatic on top analysis of single scan tracks to evaluate the laser powder bed fusion building parameters. *Materials*, *14*(18), Article 5171. https://doi.org/10.3390/ma14185171

Montgomery, D. C. (2017). *Design and analysis of experiments*. John Wiley & Sons.

Moreira, A. F., Ribeiro, K. S. B., Mariani, F. E., & Coelho, R. T. (2020). An initial investigation of Tungsten Inert Gas (TIG) torch as heat source for Additive Manufacturing (AM) process. *Procedia Manufacturing*, *48*, 671–677. https://doi.org/10.1016/j.promfg.2020.05.159

Otsu, N. (1979). A threshold selection method from gray-level histograms. *IEEE Transactions on Systems, Man, and Cybernetics, vol.* 9, no. 1, pp. 62-66, Jan. 1979, doi: 10.1109/TSMC.1979.4310076.

Pedregosa, F., Varoquaux, G., Gramfort, A., Michel, V., Thirion, B., Grisel, O., Blondel, M., Prettenhofer, P., Weiss, R., & Dubourg, V. (2011). Scikit-learn: Machine learning in Python. *The Journal of Machine Learning Research*, *12*, 2825–2830.

Raut, L. P., & Taiwade, R. V. (2021). Wire arc additive manufacturing: A comprehensive review and research directions. *Journal of Materials Engineering and Performance*, *30*(7), 4768–4791. https://doi.org/10.1007/s11665-021-05871-5

Sampson, R., Lancaster, R., Sutcliffe, M., Carswell, D., Hauser, C., & Barras, J. (2020). An improved methodology of melt pool monitoring of direct energy deposition processes. *Optics & Laser Technology*, *127* 106194. https://doi.org/10.1016/j.optlastec.2020.106194

Schwerz, C., & Nyborg, L. (2021). Linking in situ melt pool monitoring to melt pool size distributions and internal flaws in laser powder bed fusion. *Metals*, *11*(11), Article 1856. https://doi.org/10.3390/met11111856

Scipioni Bertoli, U., Wolfer, A. J., Matthews, M. J., Delplanque, J.-P. R., & Schoenung, J. M. (2017). On the limitations of volumetric energy density as a design parameter for selective laser melting. *Materials & Design*, *113*, 331–340. https://doi.org/10.1016/j.matdes.2016.10.037

Wang, J., Zhu, R., Liu, Y., & Zhang, L. (2023). Understanding melt pool characteristics in laser powder bed fusion: An overview of single- and multi-track melt pools for process optimization. *Advanced Powder Materials*, *2*(4), Article 100137. https://doi.org/10.1016/j.apmate.2023.100137

Williams, S. W., Martina, F., Addison, A. C., Ding, J., Pardal, G., & Colegrove, P. (2016). Wire + Arc Additive Manufacturing. *Materials Science and Technology*, *32*(7), 641–647. https://doi.org/10.1179/1743284715Y.0000000073

Yadroitsev, I., Thivillon, L., Bertrand, P., & Smurov, I. (2007). Strategy of manufacturing components with designed internal structure by selective laser melting of metallic powder. *Applied Surface Science*, *254*(4), 980–983. https://doi.org/10.1016/j.apsusc.2007.08.046